

High-dimensional Quantum Dynamics Study on Excitation-Specific Surface Scattering including Lattice Effects of a Five-Atoms Surface Cell

Qingyong Meng,^{1,*} Markus Schröder,^{2,†} and Hans-Dieter Meyer^{2,‡}

¹*Department of Chemistry, Northwestern Polytechnical University,*

West Youyi Road 127, 710072 Xi'an, China

²*Theoretische Chemie, Physikalisch-Chemisches Institut,*

Ruprecht-Karls Universität Heidelberg,

Im Neuenheimer Feld 229, D-69120 Heidelberg, Germany

(Dated: March 6, 2024)

Abstract

In this work high-dimensional (21D) quantum dynamics calculations on mode-specific surface scattering of a carbon monoxide molecule on a copper (100) surface with lattice effects of a five-atom surface cell are performed through the multilayer multiconfiguration time-dependent Hartree (ML-MCTDH) method. We employ a surface model in which five surface atoms near the impact site are treated as fully flexible quantum particles while all other more distant atoms are kept at fixed locations. To efficiently perform the 21D ML-MCTDH wavepacket propagation, the potential energy surface is transferred to canonical polyadic decomposition form with the aid of a Monte Carlo based method. Excitation-specific sticking probabilities of CO on Cu(100) are computed and lattice effects caused by the flexible surface atoms are demonstrated by comparison with sticking probabilities computed for a rigid surface. The dependence of the sticking probability of the initial state of the system is studied, and it is found that the sticking probability is reduced, when the surface atom on the impact site is initially vibrationally excited.

Keywords: *CO/Cu(100); ML-MCTDH; lattice effect; mode-specific; canonical polyadic decomposition*

*Electronic address: qingyong.meng@nwpu.edu.cn

†Electronic address: markus.schroeder@pci.uni-heidelberg.de

‡Electronic address: hans-dieter.meyer@pci.uni-heidelberg.de

I. INTRODUCTION

Surface scattering often leads to chemical bond ruptures, such that in-depth studies of the gas-surface dynamics, in particular its vibrational mode-specific features, are highly desirable. Molecular vibration is well known to affect the reactive probability of the gas-phase reactions, which can be predicted by the Polanyi rules [1] for few-atom reactions [2, 3]. In contrast to the gas phase, the gas-surface reactions are more complex, since molecular vibrational energy can be efficiently dissipated into the surface (or vice versa). Moreover, due to the fundamentally important role of the lattice motion in surface scattering, the surface degrees of freedom (DOFs) must be included when describing such processes in detail. This, of course, further dramatically increases the complexity of the underlying models and needs further development of the technology. In the present contribution we study mode-excitation-specific scattering of a CO molecule on a Cu(100) surface with flexible five surface atoms and compare it to scattering off a completely rigid surface model. To this end we employ a system-bath model where the CO molecule is treated as the system while the surface DOF are regarded as the bath.

Numerical calculations are performed using the Heidelberg implementation of the multiconfiguration time-dependent Hartree (MCTDH) and its multilayer extension (ML-MCTDH) [4–11]. To study mode-excitation-specific surface scattering, first ro-vibrational eigen-states of the CO are computed at a fixed distance from the Cu surface using the block-relaxation algorithm of the MCTDH program [4–8]. These eigen-states are then equipped with momentum towards the surface and propagated using the ML-MCTDH algorithm [9–11], where both, the system and bath DOFs are treated in full dimensionality. Subsequently, sticking probabilities and time-dependent expectation values of coordinates and internal energies are computed.

The efficiency of the MCTDH and ML-MCTDH algorithms in the Heidelberg implementation [4–8, 11] critically depends from a representation of the Hamiltonian as a sum-of-products (SOP) of operators that exclusively depend on one coordinate (or a small set of combined coordinates). In this work, we employ a so-called direct model for constructing the PES of the present molecule-surface problem. In this model, all DOFs, surface and CO, are included in the PES and treated on the same level. The direct model is very simple conceptionally, but the high dimensionality of the PES are often too large to build its SOP form by potfit like methods[12–14]. That is why we had developed an expansion model [15, 16], where part of the PES was developed into a Taylor series. Recently, Schröder [17] proposed a Monte Carlo method (denoted by MCCPD) to build

a CPD form of the high-dimension PES, making high-dimension dynamics calculations by the direct model possible. Moreover, the the CP format (also called CANDECOMP or PARAFAC in the literature) is more compact than the Tucker format used in potfit related methods. Hence, the new MCCPD algorithm does not only allow to re-fit higher dimensional potentials than before, but produces SOP fits which much less terms than previously. The CPU time consumed by a ML-MCTDH calculations scales almost linearly with the number of SOP terms.

The paper is organized as follows; in Section II, we will describe the theoretical framework, including the PES re-fitting calculations and quantum dynamics calculations. Section III gives the numerical details of this work. Section IV presents the flux analysis results and time-dependent expectation values, together with discussions of the present results. Finally, Section V concludes with a summary.

II. THEORETICAL FRAMEWORK

A. Hamiltonian Model

Since the geometry of the CO/Cu(100) system and the expansion model for the total Hamiltonian have been well discussed previously [15, 16, 18], only a brief description is given here. The coordinates used in this work are shown in Figure 1 (taken from reference [16]). The center atom (called “Cu1”) where the CO molecule will impact the surface as well as its four neighboring surface atoms (labeled “Cu3”, “Cu5”, “Cu6”, and “Cu8”) are taken as dynamical particles, all other Cu atoms have fixed positions. As shown in Figure 1, the coordinates of the five flexible Cu atoms are $\{\mathbf{Q}(1), \mathbf{Q}(3), \mathbf{Q}(5), \mathbf{Q}(6), \mathbf{Q}(8)\} = \mathbf{Q}$, where $\mathbf{Q}(j) = \{X_j, Y_j, Z_j\}$ are Cartesian coordinates of the j -th Cu atom. The coordinates describing the CO molecule above the surface are $\{x, y, z, r, \theta, \phi\} = \mathbf{q}$, where $\{x, y, z\}$ denote Cartesian coordinates of the center-of-mass of the CO molecule relative to the surface while $\{r, \theta, \phi\}$ denote the C-O distance as well as rotation angles of CO relative to the surface.

Having defined the coordinates in Figure 1, the total Hamiltonian $H(\mathbf{q}, \mathbf{Q})$ of the present system-bath problem is partitioned as

$$H(\mathbf{q}, \mathbf{Q}) = T + V = T_s(\mathbf{q}) + T_b(\mathbf{Q}) + V_b(\mathbf{Q}) + V_{\text{SAP}}(\mathbf{q}, \mathbf{Q}), \quad (1)$$

where T_s and T_b are the kinetic energy operators (KEO) of the CO molecule (system) and the copper surface model (bath), $V_b(\mathbf{Q})$ is the potential of the bath, while $V_{\text{SAP}}(\mathbf{q}, \mathbf{Q})$ is the 21-dimensional

SAP PES [15, 16, 18, 19] describing both, the internal system potential as well as the interaction between all system and all bath DOF.

The 15-dimensional bath potential energy $V_b(\mathbf{Q})$ is modeled as a sum of Morse potentials between Cu atoms, $M(\rho) = D[\exp(-2\alpha\rho) - 2\exp(-\alpha\rho)]$. The Morse interaction is in each Cartesian direction between nearest-neighbor atoms (including the fixed atoms, which by definition are fixed to their equilibrium position). For the out-of-plane coupling between dynamical surface atoms we used a harmonic interaction, because there is no directional preference. Then, the 15D bath potential $V_b(\mathbf{Q})$ can be written as [16]

$$\begin{aligned}
V_b(\mathbf{Q}) = V_b(Q_{1x}, \dots, Q_{8z}) = & M(Q_{3x}) + M(Q_{1x} - Q_{3x}) + M(Q_{8x} - Q_{1x}) + M(-Q_{8x}) \\
& + M(Q_{5y}) + M(Q_{1y} - Q_{5y}) + M(Q_{6y} - Q_{1y}) + M(-Q_{6y}) \\
& + M(Q_{5x}) + M(-Q_{5x}) + M(Q_{6x}) + M(-Q_{6x}) \\
& + M(Q_{3y}) + M(-Q_{3y}) + M(Q_{8y}) + M(-Q_{8y}) \\
& + M(Q_{1z}) + M(Q_{3z}) + M(Q_{5z}) + M(Q_{6z}) + M(Q_{8z}) \\
& + \frac{k}{2}(Q_{1z} - Q_{3z})^2 + \frac{k}{2}(Q_{1z} - Q_{5z})^2 + \frac{k}{2}(Q_{1z} - Q_{6z})^2 + \frac{k}{2}(Q_{1z} - Q_{8z})^2.
\end{aligned} \tag{2}$$

The parameters in $V_b(\mathbf{Q})$, *i.e.*, D , α , and k were obtained [16] by fitting the vibrationally excited energies of a clean Cu(100) surface to theoretical [20–22] and experimental [21, 23–25] vibrational energies such that the spectral properties of the bath model system resemble those of a realistic surface. Note that the bath potential is already in SOP form as required for the numerical calculations later.

According to Figure 1, the KEO of the CO system is written as (atomic units, $\hbar = 1$)

$$T_s = -\frac{1}{2m} \left(\frac{\partial^2}{\partial x^2} + \frac{\partial^2}{\partial y^2} + \frac{\partial^2}{\partial z^2} \right) - \frac{1}{2\mu} \frac{\partial^2}{\partial r^2} + \frac{1}{2mr^2} J^2(\theta, \phi), \tag{3}$$

where m is the mass of the CO molecule and μ its reduced mass. The symbol $J^2(\theta, \phi)$ denotes the operator for the squared angular momentum operating on θ and ϕ , that is

$$J^2(\theta, \phi) = -\frac{1}{\sin \theta} \frac{\partial}{\partial \theta} \left(\sin \theta \frac{\partial}{\partial \theta} \right) - \frac{1}{\sin^2(\theta)} \frac{\partial^2}{\partial \phi^2}. \tag{4}$$

Moreover, the KEO of the bath is defined as

$$T_b = -\frac{1}{2M} \sum_j \left(\frac{\partial^2}{\partial X_j^2} + \frac{\partial^2}{\partial Y_j^2} + \frac{\partial^2}{\partial Z_j^2} \right), \tag{5}$$

where M is the mass of one Cu atom. The summation in Equation (5) covers all flexible copper atoms in Figure 1.

B. The MCCPD Algorithm

The efficiency of the MCTDH algorithm in the Heidelberg implementation derives from a representation of the Hamiltonian as a SOP form of the Hamiltonian operator

$$H = \sum_r \prod_{\kappa} h_r^{(\kappa)}(q_{\kappa}) \quad (6)$$

where the constituent operators $h_r^{(\kappa)}(q_{\kappa})$ exclusively depend on one (physical or logical, *i.e.* combined) coordinate q_{κ} . Since the KEO given in Equations (3) and (5) as well as the bath potential Equation (2) are already in SOP form, only the 21D potential function, $V_{\text{SAP}}(\mathbf{q}, \mathbf{Q})$, must be recast into a SOP form. To this end we use a recently proposed method [17] for fitting a high-dimensional PES into a canonical polyadic decomposition (CPD) form, also known as PARAFAC or CANDECOMP in the literature.

The CPD form of the f -dimensional potential function $V(q_1, \dots, q_f)$ can be written as [17]

$$V(q_1, \dots, q_f) \simeq V^{\text{CPD}}(q_1, \dots, q_f) = \sum_{r=1}^R c_r v_r^{(1)}(q_1) \cdots v_r^{(f)}(q_f), \quad (7)$$

where R is the expansion order, also called the rank of the CPD expansion, while $\{q_1, \dots, q_f\}$ are the f (physical or logical) coordinates. The expansion basis functions $v_r^{(\kappa)}(q_{\kappa})$ in Equation (7), the so-called single-particle potentials (SPP), exclusively depend on one coordinate. It is assumed that the SPP are normalized, *i.e.*,

$$\langle v_r^{(\kappa)}(q_{\kappa}) | v_r^{(\kappa)}(q_{\kappa}) \rangle = 1, \quad (8)$$

but otherwise no further restrictions are imposed. It is in particular not required that the basis functions are orthogonal. Numerically, the SPP are sampled on an underlying time-independent primitive basis, typically grid points, such that Equation (7) can be re-cast into a grid-based form. Here the one-dimensional SPP function $v_r^{(\kappa)}(q_{\kappa})$ is replaced by its values evaluated on grid points, where $q_{\kappa, i_{\kappa}}$ is the i_{κ} th sampling point of the coordinate q_{κ} , and $v_{r, i_{\kappa}}^{(\kappa)} = v_r^{(\kappa)}(q_{\kappa, i_{\kappa}})$ is the SPP evaluated at this point. Then, the multidimensional potential function can be written in a tensors notation as

$$V_I^{\text{CPD}} = \sum_r c_r \prod_{\kappa} v_{r, i_{\kappa}}^{(\kappa)} = \sum_r c_r \Omega_{r, I}, \quad (9)$$

where the multi-index $I = (i_1, \dots, i_f)$ and the definition $\Omega_{r, I} = \prod_{\kappa} v_{r, i_{\kappa}}^{(\kappa)}$ have been used.

The remaining task is to find both the expansion functions and the coefficients. To this end, one starts with a set of functionals

$$\mathcal{J}_{\kappa} = \sum_I W_I^{\kappa} (V_I - V_I^{\text{CPD}})^2 + \epsilon \sum_r c_r^2 \sum_I W_I^{\kappa} \Omega_{r, I}^2, \quad (10)$$

for each mode κ , where $W_I^\kappa = 1_\kappa \sum_{i_\kappa} W_I = 1_\kappa W_{I^\kappa}^\kappa$ is a positive and coordinate-dependent weight function W_I where the κ th DOF has been integrated out and replaced by unity, and ϵ is a regularization parameter, typically set to square root of machine precision. Here, in passing, we introduced the index $I^\kappa = (i_1, \dots, i_{\kappa-1}, i_{\kappa+1}, \dots, i_f)$ which is the full combined index with the κ th sub-index missing. Note that the first part of Equation (10) measures the difference of the CPD fit to the exact potential subject to the weight function, while the second part is called the regularization for reasons that will become obvious later. It is introduced to penalize for (almost) linearly dependent terms in the CPD expansion, which may arise due to ill-conditioned matrices in the minimizing algorithm. The weight function will serve two purposes later: on the one hand it will be used to emphasize regions of interest where increased fitting accuracy is required. These will be the low energy regions where the wavefunction resides. On the other hand, the weight function will serve as a distribution function of sampling points when later the complete sum over I is replaced by Monte-Carlo sampling.

To find the minimum of Equation (10) one performs the functional derivative of \mathcal{J}_κ with respect to one SPP and coefficient of the coordinate q_κ and obtains [17]

$$\frac{\delta \mathcal{J}_\kappa}{\delta c_r v_{r,i_\kappa}^{(\kappa)}} = -2 \sum_{I^\kappa} W_{I^\kappa}^\kappa V_I \Omega_{r,I^\kappa}^\kappa + 2 \sum_{r'} c_{r'} v_{r',i_\kappa}^{(\kappa)} S_{r,r'}^\kappa + 2\epsilon c_r v_{r,i_\kappa}^{(\kappa)} S_{r,r}^\kappa = 0, \quad (11)$$

where the abbreviations

$$S_{r,r'}^{(\kappa)} = \sum_{I^\kappa} W_{I^\kappa}^{(\kappa)} \Omega_{r,I^\kappa}^\kappa \Omega_{r',I^\kappa}^\kappa, \quad (12)$$

and

$$\Omega_{r,I^\kappa}^\kappa = \prod_{\kappa' \neq \kappa} v_{r,i_{\kappa'}}^{(\kappa')} \quad (13)$$

have been used. From Equation (11), a linear equation can be found in the form [17]

$$\sum_{I^\kappa} W_{I^\kappa}^\kappa V_I \Omega_{r,I^\kappa}^\kappa = \sum_{r'} S_{r,r'}^{(\kappa)} [1 + \epsilon \delta_{r,r'}] c_r v_{r,i_\kappa}^{(\kappa)}, \quad (14)$$

that can be solved with standard linear algebra tools. This is the working equations of the present PES re-fitting process. As the solutions of the working equations (14) depend on the solutions of all other DOF one can now iteratively optimize by solving Equation (14) for each mode and using the obtained solution in the following optimization. This scheme is called alternating least squares (ALS). One should notice, however, that other than in the traditional ALS, the form given above will usually not lead to a monotonically increasing fit accuracy unless the weight function is separable [17]. In practice, however, the fit accuracy will usually increase monotonically for

an initial number of iterations before it starts to (mildly) fluctuate at which point one stops the optimization.

The main bottleneck in solving the working equations (14) is that it contains multi-dimensional quadratures over I^κ that in general cannot be separated into products of lower-dimensional integrals. If the dimensionality of the system becomes too large, these integrals cannot be completely evaluated any more. To overcome this, the complete sums are replaced by a Monte-Carlo integration, where the weight function serves as the distribution function of the sampling points $\{s^\kappa\}$ which are a sample drawn from the set of all quadrature points $\{I^\kappa\}$. With this, Equation (14) becomes

$$\sum_{s^\kappa} V_{i_\kappa s^\kappa} \Omega_{r, s^\kappa}^\kappa = \sum_{r'} Z_{r, r'}^{(\kappa)} [1 + \epsilon \delta_{r, r'}] c_r v_{r, i_\kappa}^{(\kappa)}, \quad (15)$$

with

$$Z_{r, r'}^{(\kappa)} = \sum_{s^\kappa} \Omega_{r, s^\kappa}^\kappa \Omega_{r', s^\kappa}^\kappa. \quad (16)$$

Note, that in Equation (15) the primitive grid of the mode κ is not subject to Monte-Carlo sampling such that this index is complete. We refer the reader to reference [17] for further technical details on MCCPD.

C. The MCTDH and ML-MCTDH Algorithms

In the present contribution we use the Heidelberg implementation [26] of the MCTDH algorithm, more precisely the multi-layer variant (ML-MCTDH) [9–11, 27] for solving the time-dependent Schrödinger equation. ML-MCTDH is particularly suited for treating high-dimensional systems as in the present case. The algorithm is well discussed in the literature, such that we only give a brief introduction here.

Within the ML-MCTDH algorithm the total time-dependent nuclear wavefunction is expressed in terms of a tensor in a hierarchical Tucker format which has a tree-like structure. To this end the wavefunction is expanded in a set of multi-dimensional, time-dependent basis functions, also called single particle functions (SPFs), which are themselves expanded in an underlying multi-dimensional, time-dependent basis as outlined in equation (17). This scheme is repeated until in the lowest level a time-independent primitive basis is used. The expansion can be written as

$$\varphi_m^{z-1; \kappa_{l-1}}(Q_{\kappa_{l-1}}^{z-1}, t) = \sum_{j_1}^{n_1^z} \cdots \sum_{j_{p\kappa_l}}^{n_{\kappa_l}^z} A_{m; j_1, \dots, j_{p\kappa_l}}^z(t) \prod_{\kappa_l=1}^{p^z} \varphi_{j_{\kappa_l}}^{z, \kappa_l}(Q_{\kappa_l}^z) = \sum_J A_{m; J}^z \cdot \Phi_J^z(Q_{\kappa_{l-1}}^{z-1}), \quad (17)$$

where $z = \{l; \kappa_1, \dots, \kappa_{l-1}\}$ and $z-1 = \{l-1; \kappa_1, \dots, \kappa_{l-2}\}$. The symbol l denotes the layer depth and z indicates a particular node in the ML-tree. The complete nuclear wave function Ψ , which is to be identified with φ^0 , is expanded by the time-dependent SPF with $l = 1$. The logical coordinate, $Q_{\kappa_{l-1}}^{z-1} = \{Q_1^z, \dots, Q_{p_{\kappa_l}}^z\}$, is a combination scheme of underlying coordinates Q_i . At the bottom layer the SPFs are to be replaced with time-independent primitive basis functions. The structure of an multi-layer wavefunction is most conveniently visualized by a plot of the aforementioned tree structure. The tree used in the present work is shown in Figure 2.

By inserting the multi-layer Ansatz, equation (17), into the Dirac-Frenkel variational principle, the ML-MCTDH equations of motion (EOM) for arbitrary layering schemes have been derived together with an algorithm for the recursive evaluation of all intermediate quantities entering the ML-MCTDH EOM [9–11]. According to Wang and Thoss [9], Manthe [10], and Vendrell and Meyer [11], the ML-MCTDH EOM have a very similar structure to the usual MCTDH equations, and for the top layer coefficients they are identical to the MCTDH ones, that is

$$i \frac{\partial A_I^1}{\partial t} = \sum_J \langle \Phi_I^1 | \hat{H} | \Phi_J^1 \rangle A_J^1 \quad (18)$$

where the top layer configurations

$$\Phi_J^1 = \varphi_{j_1}^{1;1}(Q_1^1, t) \cdots \varphi_{j_p}^{1;p}(Q_p^1, t), \quad (19)$$

are defined as direct products of SPFs and the multi-index $J = j_1, \dots, j_p$ has been implicitly introduced. The EOM for the propagation of the SPFs are formally the same for all layers

$$i \frac{\partial \varphi_n^{z, \kappa_l}}{\partial t} = (1 - P^{z, \kappa_l}) \sum_{j, m} (\rho^{z, \kappa_l})_{nj}^{-1} \cdot \langle \hat{H} \rangle_{jm}^{z, \kappa_l} \varphi_m^{z, \kappa_l}, \quad (20)$$

where

$$P^{z, \kappa_l} = \sum_j |\varphi_j^{z, \kappa_l}\rangle \langle \varphi_j^{z, \kappa_l}| \quad (21)$$

is the projector onto the space spanned by the φ_j^{z, κ_l} SPFs, ρ^{z, κ_l} is a density matrix and $\langle \hat{H} \rangle^{z, \kappa_l}$ is a matrix of mean-field operators acting on the φ_j^{z, κ_l} functions. In its form above, the EOM for the SPFs look identical to the usual EOM for the SPFs in the usual MCTDH [6]. Only the computation of the density matrices and mean-fields entering the EOM is now more involved than in a single-layer MCTDH scheme [9–11].

As shown above, the MCTDH and ML-MCTDH EOMs are a set of coupled non-linear differential equations, which, however, can be efficiently solved using standard numerical tools. One

may choose *propagating* an initial wave function using a real valued time variable in which case the physical evolution of the system is modeled. On the basis of the same working EOMs, one may use an imaginary time variable in which case the initial wave function is *relaxed* to the ground state of the Hamiltonian. For MCTDH (but in the Heidelberg package not for ML-MCTDH) there exist an advanced relaxation version, which allows to compute excited eigenstates. Such calculations are called improved relaxation [28] or block improved (BLK) relaxation [29]. By a BLK calculation, a set of initial wave functions is collectively relaxed to eigenstates and corresponding energy eigenvalues are obtained at one time.

III. NUMERICAL SETUP

A. Hamiltonian Operator

For representing the potential function and the wave function, we use primitive grids as detailed in Table I. The definitions of the coordinates (indicated in the first column) are given in Figure 1. We give in the second column of Table I the primitive basis functions, which underlay the DVR, together with the number of the grid points and the range of the grids in atomic units or radian. Note that the C-O distance is given by $r + r_{\min}$ where $r_{\min} = 2.1732$ Bohr is the potential minimum along r -DOF. Similarly, the z coordinate of the CO center-of-mass is $z + z_{\min}$ where $z_{\min} = 3.4771$ Bohr. Thus $r = 0$ and $z = 0$ denote equilibrium positions. In Table I, we also give the symbol of the one-dimensional (1D) function for each coordinate of the initial wave function, as well as the parameters for these 1D functions, including positions and momenta in the 1D function, frequency (ω_{HO}) and mass (M_{HO}) of a harmonic oscillator (HO) function, width of a Gaussian function (*i.e.*, variance of the modulus-square of the Gaussian function, W_{GAUSS}), and the initial quantum numbers ($j_{\text{ini}}, m_{\text{ini}}$) of the angular functions.

In Table II, we give the numerical details in the MCCPD calculations, including the number of trajectory in Monte Carlo calculations and errors of the re-fitting calculations. The present 6D MCCPD calculation is carried out through a total of $\sim 8 \times 10^6$ Monte Carlo points, resulting in re-fitting error of 10 meV. On the other hand, though similar number of Monte Carlo points, the present 21D MCCPD calculation is carried out, resulting in re-fitting error of about 48 meV. Noting that the SAP PES was constructed with a fitting error of ~ 45 meV [19], the present re-fitting errors are small enough to obtain reasonable dynamics results. Finally, the primitive grids

used in MCCPD are the same as the ones used in the ML-MCTDH calculations, and are given in Table I. In MCCPD we used the same mode combination scheme as for the wave function, the scheme is illustrated in Figure 2.

B. Preparation of initial states

In this work, both the copper surface and the CO molecule are prepared in the ro-vibrational eigen-state while the translational energy of the molecule along the z coordinate has, as in all cases, been set to $p_z = -17.0$ au, such that the molecule travels towards the surface. The resulting dynamics calculations are analyzed for initial translational energies ranging from 0.0 to 0.25 eV. To this end, total state of the system initially prepared as a product state

$$|\Psi(t=0)\rangle = \exp(ip_z z) |\Psi_{\text{CO}}\rangle |\Psi_{\text{surf}}\rangle, \quad (22)$$

where $|\Psi_{\text{CO}}\rangle$ and $|\Psi_{\text{surf}}\rangle$ are vibrational eigenfunctions of CO and Cu(100), respectively, and the exponential term accounts for the initial momentum of the CO molecule towards the Cu surface. To place the CO molecule at some distance from the surface when preparing $|\Psi_{\text{CO}}\rangle$, we added an artificial harmonic potential with the force constant of $k = 10^{-2}$ au and a minimum at $z = 4.0$ Bohr to the z -coordinate of $H_s = T_s + V_s$ and computed the states above as eigenstates of this augmented system Hamiltonian, keeping the surface as rigid. When the artificial harmonic potential is removed, the z -motion of the CO atom is no longer in an eigenstate but, after adding the initial momentum p_z , covers an energy range from zero to 0.25 eV.

One can rationalize the choice of the initial states as follows. At the distance $z = 4.0$ Bohr the interaction with the surface is negligible for disturbing the motion of the internal coordinate r . The dipole interaction between CO and surface, however, is already strong enough to break the rotational symmetry. The CO molecule becomes orientated with the C-atom pointing towards the surface. If one moves the CO molecule adiabatically from infinity to $\langle z \rangle = 4.0$ Bohr, then GS, AR, and FR correlate with the free rotational states $(j=0, m=0)$, $(j=1, m=0)$, and $(j=1, m=1)$. The states GS, BS, AR, and FR were computed using the block-improved relaxation algorithm of the Heidelberg MCTDH program. The energies of the states are reported in Table III. From there one can easily find rather good agreement between present and previous [15, 18] results. The differences are caused by the different initial z values, $z = 4.0$ Bohr in this work but $z = 0.0$ Bohr in our previous calculation [15, 18].

As initial states of the CO molecule, $|\Psi_{\text{CO}}\rangle$, we use the ground state (“GS”), the first excited state of the CO bond stretch (“BS”) as well as the first excited states associated with azimuth angle ϕ (“AR”) and frustrated zenith angle θ (“FR”) of a modified system Hamiltonian. As initial state of the surface $\Psi_{\text{surf}}(0)\rangle$ we used the ground state of the bath Hamiltonian $H_b = T_b + V_b$, which is created by imaginary time propagation of an initial Hartree product which is close to the ground state. An approximate excited surface state is subsequently created by multiplying the z -coordinate of the top Cu-atom to the ground state, that is,

$$|\Psi_{\text{surf}}^{\text{exc}}\rangle = \frac{Z_1 |\Psi_{\text{surf}}^{\text{GS}}\rangle}{\|Z_1 |\Psi_{\text{surf}}^{\text{GS}}\rangle\|}. \quad (23)$$

This creates one quanta of excitation of the out-of-plane mode of the central Cu atom. In this work, the out-of-plane excited vibrational state of the top atom in the Cu(100) surface is denoted by “surf”.

C. Analyses

With the initial state prepared according to equation (22) the CO molecule will travel towards the Cu surface where it may either be reflected and depart again or it is absorbed and sticks to the surface. The wave function of each initial state is propagate up to 10^4 fs by the ML-MCTDH method. To compute the sticking probability of the molecule on the surface we analyse the flux of the wave function fraction through the surface positioned at $z = 4.0$ Bohr. The sticking probability is obtained from $1 - P_{\text{ref}}(E)$ where $P_{\text{ref}}(E)$ is the probability of reflection at a given energy E . Beyond $z = 4.0$ Bohr we place a complex absorbing potential (CAP) [30, 31],

$$V_{\text{CAP}} = -i\eta(z - z_{\text{CAP}})^n. \quad (24)$$

The CAP absorbs the reflected part of the wave packet if it reaches the region $z \geq z_{\text{CAP}}$. In the expression of V_{CAP} , the quantities n and η are order and strength of the CAP along the coordinate z , respectively, while z_{CAP} marks the starting point of V_{CAP} . In this work, we set $n = 3$, $\eta = 0.005$ au, and $z_{\text{CAP}} = 4.5$ Bohr. Furthermore, to prevent any reflow of population from the region of the CAP back towards the surface, we add a small artificial attractive potential that sucks a wave packet deeper into the CAP region. For further technical details concerning the flux analysis we refer the reader to reference [6, 16, 32].

On the other hand, beyond the scattering probability, starting with the time-evolved wave function $|\Psi(t)\rangle$, time-dependent expectation values

$$\langle A \rangle = \frac{\langle \Psi(t) | A | \Psi(t) \rangle}{\langle \Psi(t) | \Psi(t) \rangle} \quad (25)$$

of an observable A , are possible. Illustrated in Figures 1 and 2 of the Supporting Information are time-dependent norms $\langle \Psi(t) | \Psi(t) \rangle$ of the present ML-MCTDH wave functions. The time-dependent norm becomes less than one for $t > 500$ fs, what makes the interpretation of the expectation values difficult, because the CAP annihilates predominantly the fast-moving long-ranged parts of the wave packet. We therefore show expectation values only for times up to 500 fs. In this work, we used the following observable operators: the CO total energy $H_s = T_s + V_{SAP}(\mathbf{q}, 0)$, the surface energy, $H_b = T_b + V_b$, the distance of CO from the surface, Z , and the out-of-plane motion of the top Cu-atom, Z_1 .

IV. RESULTS AND DISCUSSIONS

A. Rigid Surface

With the various initial states as discussed in Section III B, extensive ML-MCTDH propagations and follow-up flux and expectation analyses (see Section III C) are performed to compute the sticking probabilities. In this section, we shall show results obtained with the 6D Hamiltonian model, *i.e.* scattering off a rigid surface. Figure 3 displays the sticking probabilities as a function of the collision energies for the different initial states. One observes that the sticking probabilities drop quickly to small values for the collision energies above 0.03 eV (~ 240 cm⁻¹). For the rotational excited states, AR and FR, there is a small recovery of the sticking between 0.03 and 0.15 eV, but above 0.15 eV almost all incoming particles are reflected. Since in the present model the Cu(100) surface is rigid, the collision energy cannot be transferred to surface DOFs. To accomplish sticking, the incoming translational energy has to be partially transferred to xy -motion (T mode), or to $\theta\phi$ -motion (frustrated rotation, R mode).

When the CO molecule approaches the surface, it is accelerated by about 0.4 eV due to the attractive part of the interaction potential. Near and slightly above $t = 200$ fs the wavepacket is closest to the surface (compare with Figure 4). Figure 5 shows the kinetic energy of the xy -motion for four initial states versus time. Near $t = 200$ fs the energy rises sharply, then there is a small back-transfer of energy, and in the end between 27 and 48 meV are transferred to motion parallel

to the surface. The increase of the expectation values for $t > 450$ fs is due to the decrease in norm as discussed above.

The energy transfer is smallest, if the CO molecule is initially in its ro-vibrational ground state. The elongation of the C-O bond, due to a vibrational excitation, helps to enhance the energy transfer to parallel motion. But more efficiently this energy transfer is enhanced by initial rotational excitations. The CO rotational energy over time is shown in Figure 5 of the Supporting Information. During the collision there is a virtual rotational excitation of $15 \sim 30$ meV, but the final energy transfer is smaller than 10 meV. Again, initial rotational excitation enhances the energy transfer, but it remains small. Hence the sticking on a rigid surface is mainly due to energy transfer to parallel motion.

B. Flexible Surface

In Figure 6 is shown the sticking probabilities of the 21D results from the direct model. The sticking probabilities decrease much more slowly compared to the case of rigid surface discussed in Section IV A, but they start to decay quickly for collision energies above 0.15 eV.

The figure shows sticking probabilities, which separate into two categories. First, an excitation of the out-of-plane mode of the center atom attenuates the sticking process, and the corresponding 21D sticking probability (red line, denoted by “surf”). has the smallest values. Obviously, a vibrational excitation of surface atoms helps to kick-off the CO molecule from the surface. Second, the sticking probabilities computed for vibrationally or rotationally excited states of the CO molecule are close to each other. The initial ro-vibrational state of CO is less relevant.

The importance of the bath is demonstrated by Figure 7, which shows the expectation energy of the bath Hamiltonian versus collision time. During the collision the bath absorbs about 0.21 eV, which is much more compared to the energy going into parallel motion (compare with Figure 5). This large energy transfer explains the large sticking probability. The two lower lines in Figure 7 display the energy expectation value of the out-of-plane motion of the top Cu-atom. This motion absorbs about 0.13 eV, that is more than half of the energy transferred to the bath is taken by the out-of-plane motion of the top Cu-atom.

C. Discussions

In Figure 8 the computed sticking probabilities of the CO molecule in its ro-vibrational ground state are compared for the model with rigid and with flexible surface atoms, respectively. As shown in Figure 8, at collision energies below 0.15 eV the sticking probability of the model with flexible surface atoms shows a very slow decrease, in contrast to the case where all surface atoms are fixed. Further increasing the collision energy to above 0.15 eV let the sticking probability for flexible surface atoms start to decrease and to reach zero when the collision energy is above 0.20 eV. In any case, the sticking probability is much larger when the surface atoms are treated as flexible atoms as compared to the case when all surface atoms are fixed. This difference is caused by the surface DOFs that let the CO molecule transfer translational kinetic energy to other modes, in particular to the bath modes. Hence the surface DOFs play an important role in surface scattering.

To visualize the dynamics behavior of the surface scattering of CO, we show the time-dependent expectation values of the z -coordinate of CO and (if present) of the top Cu atom in Figure 4. In the case of a rigid surface (the black line), the CO molecule collides with the surface near 200 fs, where the position of CO almost reaches $z = 0$. Remember that $z = 0$ is the equilibrium position of a CO atom adsorbed on the surface. As the displayed value is an expectation value averaged over the wavepacket, large parts of the wavepacket have entered the region $z < 0$ where a strong repulsion sets in. The wavepacket is thus reflected and the z value increases again. Above $t = 400$ fs the z curve flattens and starts to turn back. This is an artifact caused by the CAP absorption, which sets in at $t = 400$ fs. As the distant parts of the wavepacket are annihilated by the CAP, the average z value is reduced.

In the case of a flexible surface (blue lines), the situation changes. Since the attractive interaction between the center and flanking copper atoms, the center atom slightly moves upwards and is then pushed downwards by the hard collision with CO. The z turning point occurs at about 220 fs, which is slightly larger compared to the collision with a rigid surface. After the collision the z expectation value increases much slower as in the case of a rigid surface. This is because a large fraction of the wavepacket remains close to the surface. Above 400 fs the expectation value is again distorted by the absorption due to the CAP. After the collision, the center surface atom performs an oscillatory motion, which is slightly damped due to the coupling to the other surface atoms. Near $t = 330$ fs, when the Z coordinate assumes its maximum value, the center

atom pushes out some of the part of the wavepacket, which has remained close to the surface. This back-transfer of bath energy, which can also be observed in Figure 7, reduces the sticking probability.

V. CONCLUSIONS

To study mode-specific features in surface scattering of CO/Cu(100) with lattice effects, a surface model with five flexible copper atoms is employed and the ML-MCTDH method is used to perform the quantum dynamics calculations. To perform the ML-MCTDH calculations efficiently, the potential terms are firstly re-fitted to the CPD form using the Monte Carlo method by the MCCPD method [17].

The first few ro-vibrational states of CO fixed at a distance from the surface are computed and serve as initial states of the ML-MCTDH propagations. On the basis of these calculations, we find that the sticking probabilities are strongly affected by the inclusion of movable surface atoms, but depend only weakly on initial ro-vibrational states of CO. The sticking probability is reduced, if the out-of-plane motion of the top atom is initially excited, compared to a surface in its vibrational ground state. With the aid of the time-dependent expectation values the scattering process is further analyzed.

Supplementary Material

See Supplementary Material Documents at <http://dx.doi.org/XXX> for details of the results of the expectation analyses.

Acknowledgments

Q.M. gratefully acknowledges financial support by National Natural Science Foundation of China (Grant No. 21773186), National Natural Science Foundation of Shaanxi Province (Grant No. 2019JM-380), Fundamental Research Funds for the Central Universities (Grant No. 3102017JC01001), and Hundred-Talent Program of Shaanxi. M.S. and H.-D.M. gratefully acknowledges financial support by the *Deutsche Forschungsgemeinschaft* (DFG) project ME623/22-1. The authors wish to thank Prof. Dr. R. Marquardt (Strasbourg, France) for providing us their

- [1] J. C. Polanyi and W. H. Wong. Location of Energy Barriers. I. Effect on the Dynamics of Reactions $A + BC$. *J. Chem. Phys.* **51** (1969), 1439–1450.
- [2] C. Xiao, X. Xu, S. Liu, T. Wang, W. Dong, T. Yang, Z. Sun, D. Dai, X. Xu, D. H. Zhang, and X. Yang. Experimental and Theoretical Differential Cross Sections for a Four-Atom Reaction: $HD + OH \rightarrow H_2O + D$. *Science* **333** (2011), 440–442.
- [3] T. Yang, J. Chen, L. Huang, T. Wang, C. Xiao, Z. Sun, D. Dai, X. Yang, and D. H. Zhang. Extremely Short-lived Reaction Resonances in $Cl + HD (\nu = 1) \rightarrow DCl + H$ due to Chemical Bond Softening. *Science* **347** (2015), 60–63.
- [4] H.-D. Meyer, U. Manthe, and L. S. Cederbaum. The Multi-Configurational Time-Dependent Hartree Approach. *Chem. Phys. Lett.* **165** (1990), 73–78.
- [5] U. Manthe, H.-D. Meyer, and L. S. Cederbaum. Wave-Packet Dynamics within the Multiconfiguration Hartree Framework: General Aspects and application to $NOCl$. *J. Chem. Phys.* **97** (1992), 3199–3213.
- [6] M. H. Beck, A. Jäckle, G. A. Worth, and H.-D. Meyer. The Multi-Configuration Time-Dependent Hartree (MCTDH) Method: A Highly Efficient Algorithm for Propagating Wave Packets. *Phys. Rep* **324** (2000), 1–105.
- [7] H.-D. Meyer, F. Gatti, and G. A. Worth, Eds. *Multidimensional Quantum Dynamics: MCTDH Theory and Applications*. Wiley-VCH, Weinheim, 2009.
- [8] H.-D. Meyer. Studying Molecular Quantum Dynamics with the Multi-Configuration Time-Dependent Hartree Method. *WIREs: Comput. Mol. Sci.* **2** (2012), 351–374.
- [9] H. Wang and M. Thoss. Multilayer Formulation of the Multiconfiguration Time-Dependent Hartree Theory. *J. Chem. Phys.* **119** (2003), 1289–1299.
- [10] U. Manthe. A Multilayer Multiconfigurational Time-Dependent Hartree Approach for Quantum Dynamics on General Potential Energy Surfaces. *J. Chem. Phys.* **128** (2008), 164116.
- [11] O. Vendrell and H.-D. Meyer. Multilayer Multiconfiguration Time-Dependent Hartree Method: Implementation and Applications to a Henon-Heiles Hamiltonian and to Pyrazine. *J. Chem. Phys.* **134** (2011), 044135.
- [12] A. Jäckle and H.-D. Meyer. Product Representation of Potential Energy Surfaces. *J. Chem. Phys.* **104** (1996), 7974.

- [13] D. Peláez and H.-D. Meyer. The Multigrid POTFIT (MGPF) Method: Grid Representations of Potentials for Quantum Dynamics of Large Systems. *J. Chem. Phys.* **138** (2013), 014108.
- [14] M. Schröder and H.-D. Meyer. Transforming High-Dimensional Potential Energy Surfaces into Sum-of-Products form using Monte Carlo Methods. *J. Chem. Phys.* **147** (2017), 064105.
- [15] Q. Meng and H.-D. Meyer. Expansion Hamiltonian Model for a Diatomic Molecule Adsorbed on a Surface: Vibrational States of the CO/Cu(100) System including Surface Vibrations. *J. Chem. Phys.* **143** (2015), 164310.
- [16] Q. Meng and H.-D. Meyer. Lattice Effects of Surface Cell: Multilayer Multiconfiguration Time-Dependent Hartree Study on Surface Scattering of CO/Cu(100). *J. Chem. Phys.* **146** (2017), 184305.
- [17] M. Schröder. Transforming High-Dimensional Potential Energy Surfaces into a Canonical Polyadic Decomposition using Monte Carlo Methods. *J. Chem. Phys.* **152** (2020), 024108.
- [18] Q. Meng and H.-D. Meyer. MCTDH Study on Vibrational States of the CO/Cu(100) System. *J. Chem. Phys.* **139** (2013), 164709.
- [19] R. Marquardt, F. Cuvelier, R. A. Olsen, E. J. Baerends, J. C. Tremblay, and P. Saalfrank. A New Analytical Potential Energy Surface for the Adsorption System CO/Cu(100). *J. Chem. Phys.* **132** (2010), 074108.
- [20] A. D. Corso. Density-Functional Perturbation Theory with Ultrasoft Pseudopotentials. *Phys. Rev. B* **64** (2001), 235118.
- [21] R. Heid and K.-P. Bohnen. *Ab initio* Lattice Dynamics of Metal Surfaces. *Phys. Rep.* **387** (2003), 151–213.
- [22] S. D. Borisova, S. V. Eremeev, G. G. Rusina, V. S. Stepanyuk, P. Bruno, and E. V. Chulkov. Vibrations of Small Cobalt Clusters on Low-Index Surfaces of Copper: Tight-Binding Simulations. *Phys. Rev. B* **78** (2008), 075428.
- [23] M. Wuttig, R. Franchy, and H. Ibach. The Rayleigh Phonon Dispersion on Cu(100): A Stress Induced Frequency Shift? *Z. Phys. B* **65** (1986), 71–74.
- [24] M. Wuttig, R. Franchy, and H. Ibach. The Rayleigh Phonon Dispersion Curve on Cu(100) in the GX Direction. *Solid State Communications* **57** (1986), 445 – 447.
- [25] Y. Chen, S. Y. Tong, J.-S. Kim, L. L. Kesmodel, T. Rodach, K. P. Bohnen, and K. M. Ho. Characterization of Surface Phonons on Cu(001) and Ag(001): First-Principles Phonon Calculations with Experimental and Theoretical Studies of High-Resolution Electron-Energy-Loss Spectra. *Phys. Rev. B* **44** (1991), 11394–11401.

- [26] G. A. Worth, M. H. Beck, A. Jäckle, O. Vendrell, and H.-D. Meyer. The MCTDH Package, Version 8.2, (2000). H.-D. Meyer, Version 8.3 (2002), Version 8.4 (2007). O. Vendrell and H.-D. Meyer Version 8.5 (2013). Version 8.5 contains the ML-MCTDH algorithm. Current versions: 8.4.18 and 8.5.11 (2019). See <http://mctdh.uni-hd.de/>.
- [27] H. Wang. Multilayer Multiconfiguration Time-Dependent Hartree Theory. *J. Phys. Chem. A* **119** (2015), 7951.
- [28] H.-D. Meyer, F. Le Quéré, C. Léonard, and F. Gatti. Calculation and Selective Population of Vibrational Levels with the Multiconfiguration Time-Dependent Hartree (MCTDH) Algorithm. *Chem. Phys.* **329** (2006), 179–192.
- [29] L. J. Doriol, F. Gatti, C. Iung, and H.-D. Meyer. Computation of Vibrational Energy Levels and Eigenstates of Fluoroform using the Multiconfiguration Time-Dependent Hartree Method. *J. Chem. Phys.* **129** (2008), 224109.
- [30] U. V. Riss and H.-D. Meyer. Calculation of Resonance Energies and Widths using the Complex Absorbing Potential Method. *J. Phys. B* **26** (1993), 4503.
- [31] U. V. Riss and H.-D. Meyer. Investigation on the Reflection and Transmission Properties of Complex Absorbing Potentials. *J. Chem. Phys.* **105** (1996), 1409.
- [32] A. Jäckle and H.-D. Meyer. Time-Dependent Calculation of Reactive Flux Employing Complex Absorbing Potentials: General Aspects and Application within MCTDH. *J. Chem. Phys.* **105** (1996), 6778.
- [33] S. Sukiasyan and H.-D. Meyer. On the Effect of Initial Rotation on Reactivity. A Multi-Configuration Time-Dependent Hartree (MCTDH) Wave-Packet Propagation Study on the $\text{H} + \text{D}_2$ and $\text{D} + \text{H}_2$ Reactive Scattering Systems. *J. Phys. Chem. A* **105** (2001), 2604–2611.
- [34] C. J. Hirschmugl, G. P. Williams, F. M. Hoffmann, and Y. J. Chabal. Adsorbate-Substrate Resonant Interactions Observed for CO on Cu(100) in the Far Infrared. *Phys. Rev. Lett.* **65** (1990), 480–483.
- [35] J. Ellis, J. P. Toennies, and G. Witte. Helium Atom Scattering Study of the Frustrated Translation Mode of CO Adsorbed on the Cu(001) Surface. *J. Chem. Phys.* **102** (1995), 5059–5070.
- [36] A. P. Graham, F. M. Hoffmann, J. P. Toennies, G. P. Williams, C. Hirschmugl, and J. Ellis. A High Resolution Helium Atom Scattering and Far Infrared Study of the Dynamics and the Lateral Potential Energy Surface of CO Molecules Chemisorbed on Cu(001). *J. Chem. Phys.* **108** (1998), 7825.

TABLE I: DVR-grids used in the dynamics calculations, and parameters of the initial wave function for the ML-MCTDH propagation calculations. The definitions of the coordinates (indicated in the first column) are given in Figure 1(b) as well as Figure 1 of reference [15]. The second column describes the primitive basis functions, which underlay the DVR. The third column gives the number of the grid points. The fourth column gives the range of the grids in atomic unit or radian. Note that the C-O distance is given by $r + r_{\min}$ where $r_{\min} = 2.1732$ Bohr is the potential minimum along r -DOF. Similarly, the z coordinate of the CO center of mass is $z + z_{\min}$ where $z_{\min} = 3.4771$ Bohr. Thus $r = 0$ and $z = 0$ denote equilibrium positions. The fifth column gives the symbol of the one-dimensional (1D) function for each coordinate of the initial wave function. The other columns give the parameters for these 1D functions, including positions and momenta in the 1D function, frequency (ω_{HO}) and mass (M_{HO}) of the HO function, width of the GAUSS function (*i.e.*, variance of the modulus-square of the Gauss function, W_{GAUSS}), and the initial quantum numbers (j_{ini} , m_{ini}) of the angular functions.

| Coordinates ^a | Primitive basis function | | | Initial wave function | | |
|--|--------------------------|-------------|---------------------|-----------------------|----------|---|
| | Symbol ^b | Grid points | Range of the grids | Symbol ^c | Position | Momentum |
| <i>Coordinates of the CO molecule, q</i> | | | | | | |
| x and y | EXP | 45 | $[-2.415, 2.415]$ | HO | 0.0 | 0.0 $\omega_{\text{HO}} = 31.8 \text{ cm}^{-1}$, $M_{\text{HO}} = 28.0 \text{ AMU}$ |
| z | FFT | 192 | $[-1.000, 6.000]$ | GAUSS | 4.0 | -17.0 width = 0.1 |
| r | HO | 21 | $[-0.300, 0.300]$ | EIGENF | — | — ground state |
| θ | PLEG | 45 | $[0, \pi]$ | KLEG | — | — $j_{\text{ini}} = j$ |
| ϕ | EXP | 27 | $[0, 2\pi]$ | K | — | — $m_{\text{ini}} = m$ |
| <i>Coordinates of the Cu atoms, Q_i</i> | | | | | | |
| Q_{1z} | SIN | 55 | $[-0.800, 1.200]$ | HO | 0.0 | 0.0 $\omega_{\text{HO}} = 103.4 \text{ cm}^{-1}$, $M_{\text{HO}} = 63.546 \text{ AMU}$ |
| $Q_{i\alpha}$ | HO | 15 | $[-0.397, 0.397]^d$ | HO | 0.0 | 0.0 $\omega_{\text{HO}} = 103.4 \text{ cm}^{-1}$, $M_{\text{HO}} = 63.546 \text{ AMU}$ |
| Q_{jz} | HO | 15 | $[-0.397, 0.397]^d$ | HO | 0.0 | 0.0 $\omega_{\text{HO}} = 103.4 \text{ cm}^{-1}$, $M_{\text{HO}} = 63.546 \text{ AMU}$ |

^a Indices in $Q_{i\alpha}$ are $i = 1, 3, 5, 6, 8$ and $\alpha = x, y$, while index in Q_{jz} is $j = 3, 5, 6, 8$.

^b “EXP”, “SIN”, and “HO” stand for exponential, sine, and harmonic oscillator DVR, respectively. “FFT” denotes fast Fourier transform collocation. “PLEG” denotes a two-dimensional extended Legendre DVR [33] for angular coordinates.

^c “HO” and “GAUSS” designate the choice of harmonic oscillator eigenfunction and Gaussian function, respectively, as initial SPFs. EIGENF means eigenfunction of a specified potential which, in this work, is SAP potential along r setting z is sufficiently large ($z = 4.0$ Bohr) as to make the interaction between CO and Cu(100) negligible. “KLEG” and “K” denotes associated Legendre function and body-fixed magnetic quantum number, respectively, to specify the initial wavefunction.

^d In these cases only the position (that is 0.0) and frequency (that is 103.4 cm^{-1}) parameters of the HO DVR are given, and then the ranges of the grids are calculated automatically.

TABLE II: Numerical details of the present MCCPD calculations [17]. The first column gives the method used in the present Monte-Carlo sampling. The second column gives the temperature ($k_B T$ in eV) of each kind Metropolis sampling. These samplings are distributed according to the weight $w(\mathbf{q}, \mathbf{Q}) = \exp(-V_{\text{SAP}}(\mathbf{q}, \mathbf{Q})/(k_B T))$. The third and fourth columns present the numbers of the sampling points used for the fit and test, respectively. For the CPD fit the combined set of sampling points of the four distributions given in the FIT column are used. The computation of the fit error is performed for each temperature distribution individually, and for all test points all together. Note that fit- and test-distributions are independent. The fifth and sixth columns give energy errors (in meV) between refitted and original potential using test sampling points, including their average (denoted by MEAN) and root-mean-square (denoted by RMS) values, respectively.

| | Trajectory | | | | Testing Error (meV) | |
|-----------------|------------|--------------|--------------------|--------------------|------------------------|-------|
| | Method | $k_B T$ (eV) | FIT | TEST | MEAN | RMS |
| <i>6D PES</i> | | | | | | |
| | Metropolis | 0.05 | 6.00×10^5 | 1.00×10^6 | -3.58×10^{-4} | 0.50 |
| | Metropolis | 0.25 | 3.00×10^5 | 1.00×10^6 | -2.22×10^{-2} | 1.75 |
| | Metropolis | 0.50 | 1.00×10^5 | 1.00×10^6 | -3.21×10^{-3} | 4.12 |
| | Metropolis | 1.00 | | 1.00×10^6 | 3.14×10^{-2} | 9.77 |
| | Metropolis | 1.50 | | 1.00×10^6 | 2.52×10^{-2} | 12.44 |
| | Metropolis | 2.50 | | 1.00×10^6 | 4.02×10^{-3} | 14.11 |
| | uniform | | 5.00×10^4 | 1.00×10^6 | -2.26×10^{-2} | 17.79 |
| <i>in total</i> | | | 1.05×10^6 | 7.00×10^6 | 1.76×10^{-3} | 10.06 |
| <i>21D PES</i> | | | | | | |
| | Metropolis | 0.05 | 2.00×10^5 | 1.00×10^6 | 0.36 | 18.30 |
| | Metropolis | 0.25 | 1.05×10^5 | 1.00×10^6 | 0.15 | 29.08 |
| | Metropolis | 0.50 | 5.00×10^4 | 1.00×10^6 | 1.03 | 33.44 |
| | Metropolis | 1.00 | | 1.00×10^6 | 0.58 | 47.61 |
| | Metropolis | 1.50 | | 1.00×10^6 | 0.15 | 54.96 |
| | Metropolis | 2.50 | | 1.00×10^6 | -0.37 | 60.95 |
| | uniform | | 5.00×10^4 | 1.00×10^6 | -2.02 | 70.92 |
| <i>in total</i> | | | 4.50×10^5 | 7.00×10^6 | -1.63×10^{-2} | 48.30 |

TABLE III: Excitation energies of the first excited states (all energies in cm^{-1}) of the CO bond stretch (denoted by BS) as well as the Azimuth and frustrated rotation (denoted by AR and FR) based on the MCTDH relaxation calculations, where the initial CO molecule is located at $z = 4.0$ au. The excitation energies of the overtone states of these modes are also given. For comparison, the previous excitation energies for the CO molecule adsorbed on the surface are also shown. The first and second columns give the vibrational modes and corresponding symbols of the system. The third column present the present MCTDH relaxation results at the 6D $\{x, y, z, r, \theta, \phi\}$ level. The other three columns give the previous theoretical and experimental results for the excitation energies of CO adsorbed on the surface.

| Mode | Symbol | $\langle z \rangle = 4 \text{ Bohr}^a$ | $\langle z \rangle = 0, \text{ adsorbed}^b$ | | |
|--------------------------------------|---------|--|---|----------------------|--------------------|
| | | MCTDH | MCTDH ^c | Lanczos ^d | Expt. ^e |
| C-O stretch | BS | 2141.2 | 2046.5 | 2052.5 | 2079.3 |
| Azimuth rotation | AR | 48.2 | — | — | — |
| Frustrated rotation | FR | 92.2 | 366.1 | 366.1 | 345.2 |
| C-O stretch with azimuth rotation | BS + AR | 2189.4 | — | — | — |
| C-O stretch with Frustrated rotation | BS + FR | 2233.2 | 2412.6 | 2418.6 | 2424.5 |

^a The present work, where the CO molecule is located at $\langle z \rangle = 4.0$ au with the aid of an augmented harmonic potential (see the maintext).

^b The previous work, where the CO molecule is adsorbed on the Cu(100) surface.

^c Reference [18].

^d Reference [19].

^e Reference [34–36].

Figure Captions

Figure 1: (a) Definition of the atomic arrangement of the CO/Cu(100) system. The red and gray circles represent the oxygen and carbon atoms, respectively, and the pink circles represent the copper atoms. Coordinates of CO, center copper atom (called Cu1), and four non-center copper atoms (called Cu3, Cu5, Cu6, and Cu8) nearest to Cu1 are involved in calculations. These five copper atoms are selected from a larger nine-by-nine atoms grid, in which the copper atoms are ordered in three planes (layers) perpendicular to the z -axis. For clarity, the four second-nearest copper atoms (called Cu2, Cu4, Cu7, and Cu9) in the surface layer are also shown. In subfigure (b) we show the definitions of the system-coordinates in this work. The origin of the Cartesian coordinate system is the equilibrium position of the top atom Cu1. Here $\{x, y, z\}$ are the Cartesian coordinates of the center-of-mass (denoted by G) of the CO molecule. Variable r is the bond length of the CO molecule. Variable θ is the polar angle between C-O bond and the z axis, whereas ϕ is the azimuthal angle. The figure is reprinted with permission from *J. Chem. Phys.* **146**, 184305 (2017). Copyright 2017 American Institute of Physics.

Figure 2: The ML-tree used in the 21D calculations. Each circle represents a node and the squares represent the primitive basis functions, i.e. the grids. The numbers on the lines between the circles represent the numbers of SPFs used on the node, and the numbers between a circle and a square are the number of grid points used for the particular DOF. This is a four layer tree ($l=4$).

Figure 3: Sticking probabilities versus collision energy (in eV) computed for the 6D model which has coordinates $\{x, y, z, r, \theta, \phi\}$. The black and red lines represent the sticking probabilities when CO is initially in its ground state (denoted by GS) and in the first vibrationally excited state of the C-O stretch mode (denoted by BS). The blue and green lines represent those of excited states associated with frustrated azimuth angle ϕ (denoted by FR) and zenith angle θ (denoted by AR), respectively.

Figure 4: Comparison of the time-dependent position expectation values along the z coordinate of CO (the solid lines) and the top copper atom (the dashed line). The red and blue lines represent the results from 6D (i. e. rigid surface) and 21D models, respectively. The initial ro-vibrational

state of CO is its ground state.

Figure 5: Kinetic energy of the motion parallel to the surface versus collision time. The four lines refer to different ro-vibrational initial states of CO. A rigid surface is used (6D model). The increase of the energy for times $t > 400$ fs is an artifact. The wavepacket reaches the CAP at $t = 400$ fs and the norm decreases sharply thereafter. The parts of the wavepacket which are close to the surface get a higher weight when evaluating the expectation value for times larger than 400 fs. In general, it is difficult to interpret expectation values after CAP absorption has set in.

Figure 6: Sticking probabilities versus collision energy (in eV) computed for the 21D model with flexible surface atoms. The black and green lines represent the sticking probabilities when the CO molecule is initially in the ground state (denoted by GS) and vibrational excited state of the CO bond stretch mode (denoted by BS), the yellow and blue lines represent those where the molecule is in the excited states associated with frustrated azimuth angle ϕ (denoted by AR) and zenith angle θ (denoted by FR), respectively. The red line represents the sticking probability when the molecule is initially in the ground state but the surface is in the excited state associated with the out-of-plane mode of the center atom (denoted by surf).

Figure 7: Energy of the bath versus collision time. Initially the CO molecule is in its ro-vibrational ground (black line) state or in the rotationally excited FR state (blue line). The two dashed lines show the energy expectation value of the Z-motion of the top Cu-atom.

Figure 8: Comparison of the sticking probabilities for the 6D (red line), 21D (blue line), and 21D (green line) models, where all sticking probabilities are computed with CO initially in its ground state.

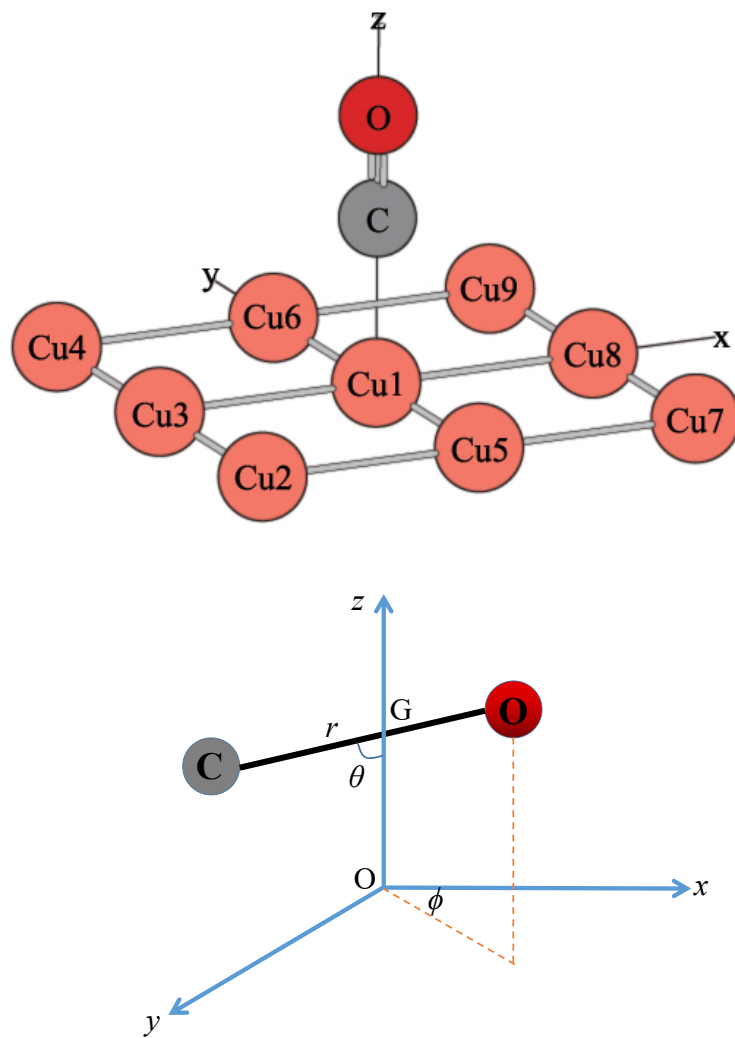
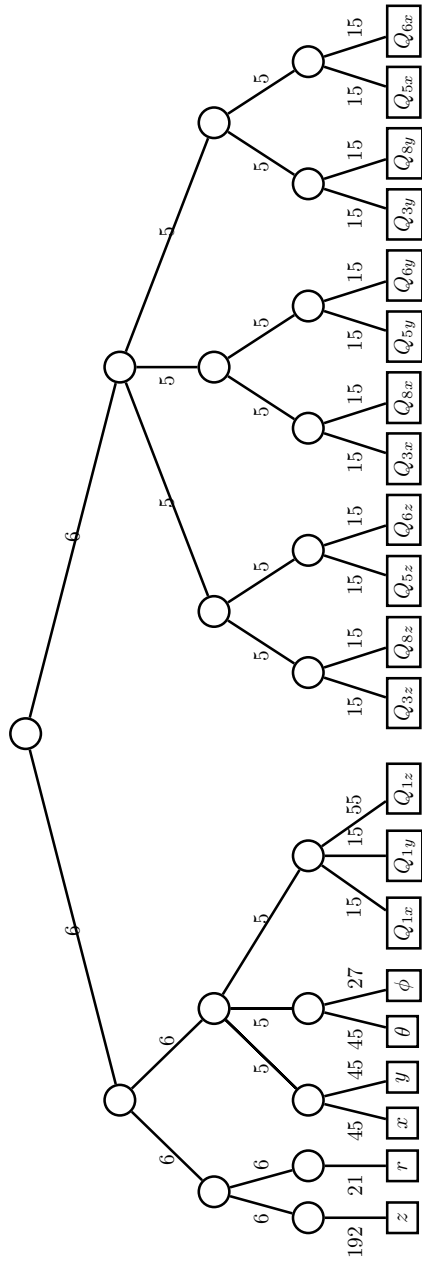


FIG. 1: CO/Cu, 21D MCCPD



26
FIG. 2: CO/Cu, 21D MCCPD

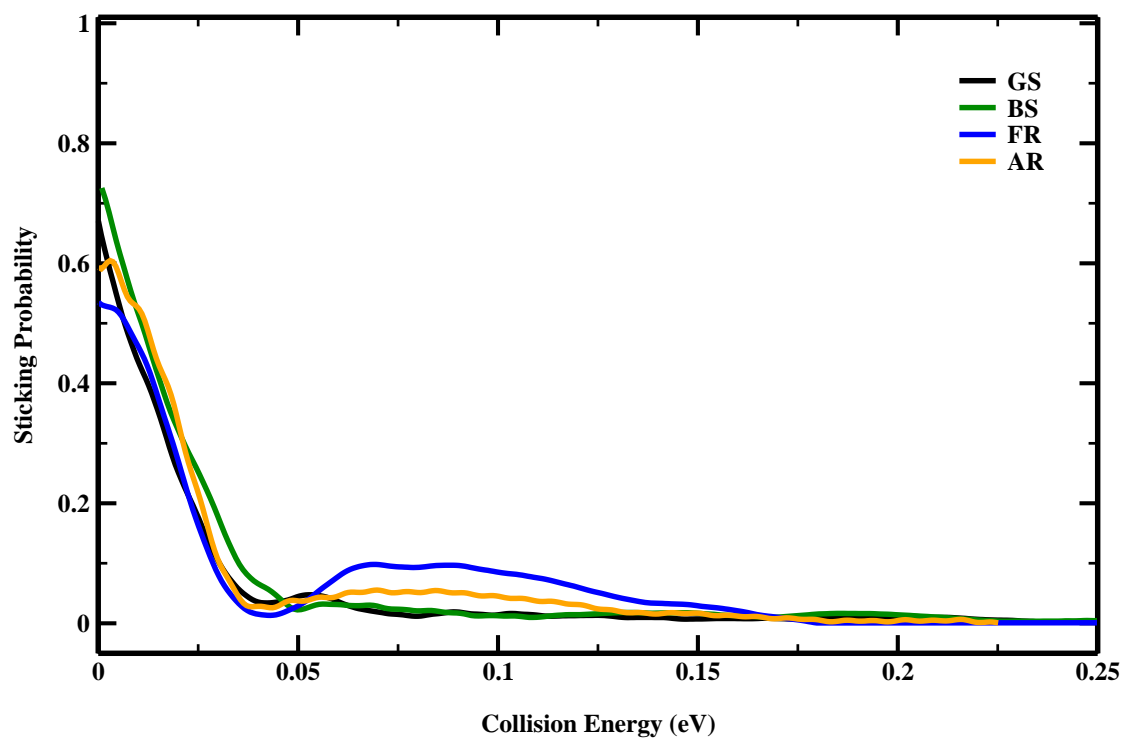


FIG. 3: CO/Cu, 21D MCCPD

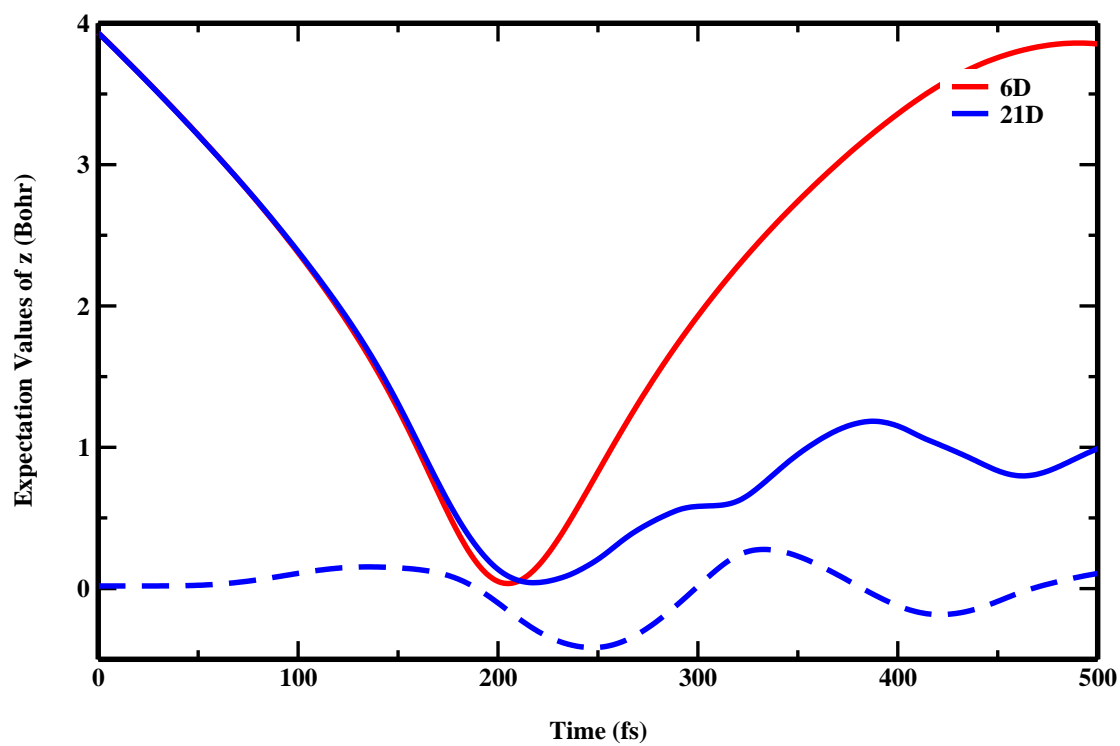


FIG. 4: CO/Cu, 21D MCCPD

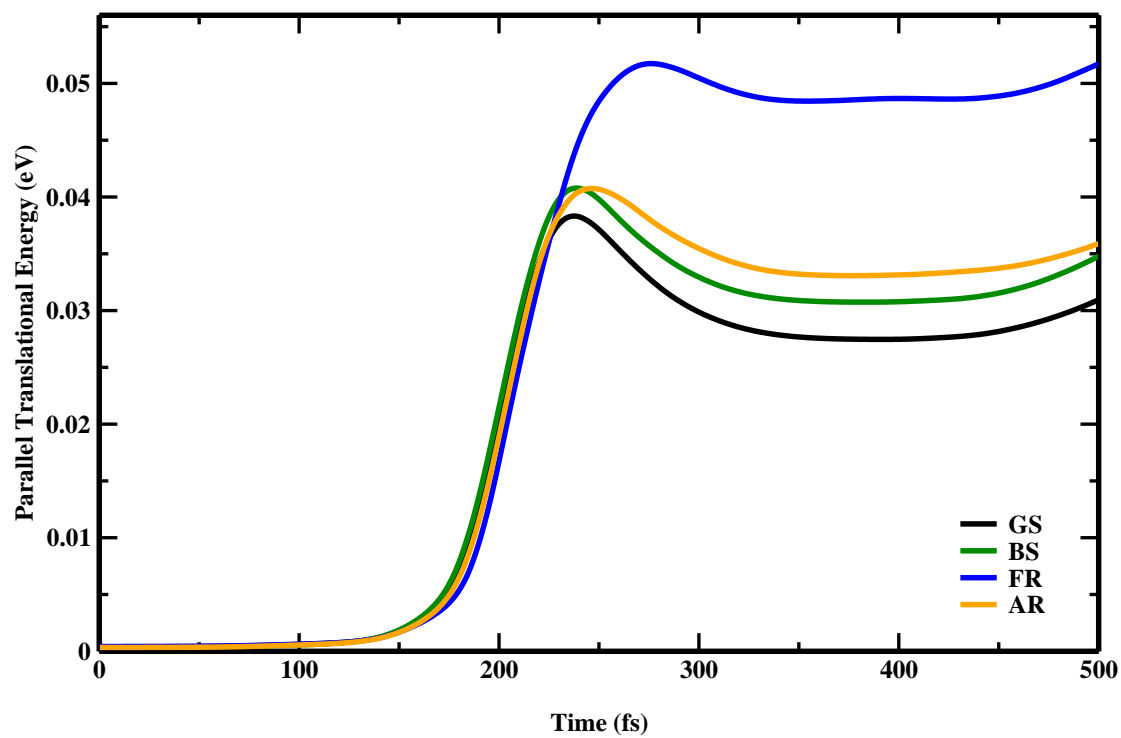


FIG. 5: CO/Cu, 21D MCCPD

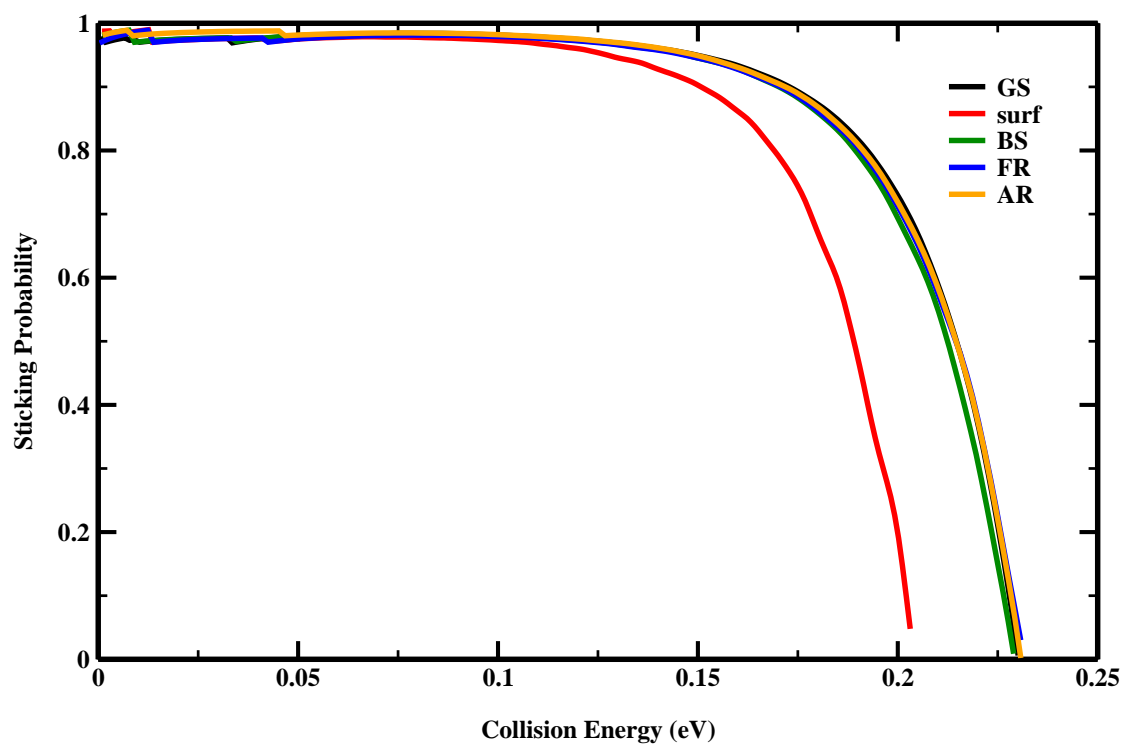


FIG. 6: CO/Cu, 21D MCCPD

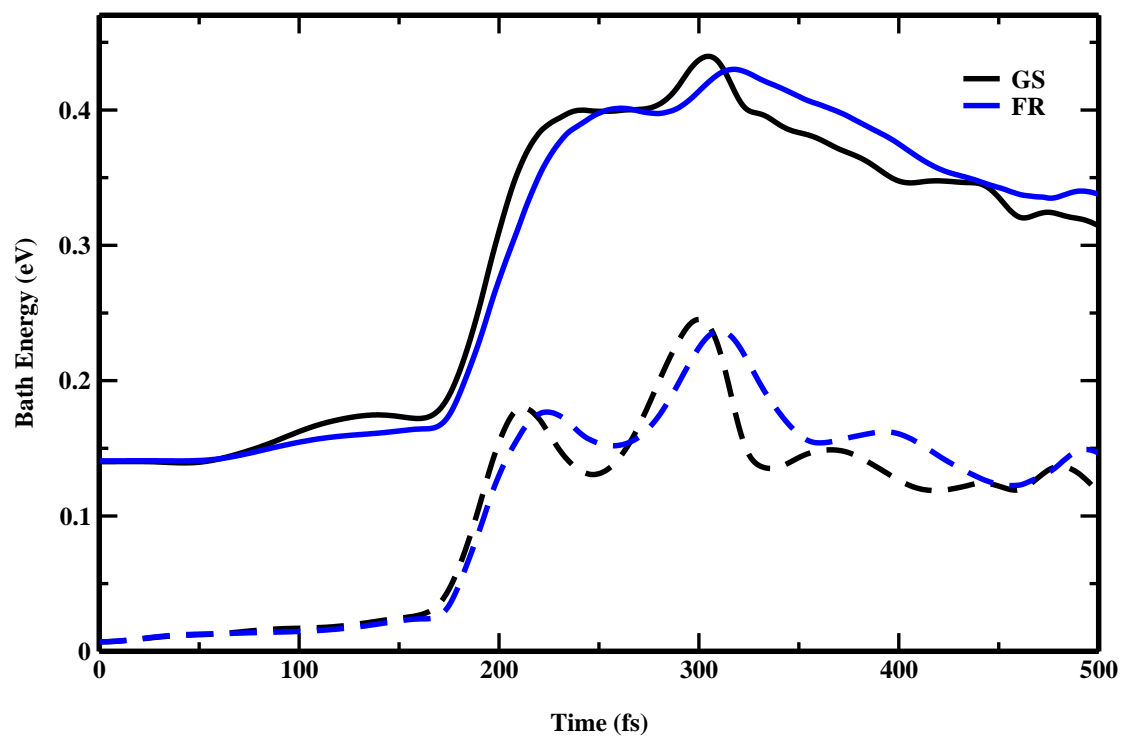


FIG. 7: CO/Cu, 21D MCCPD

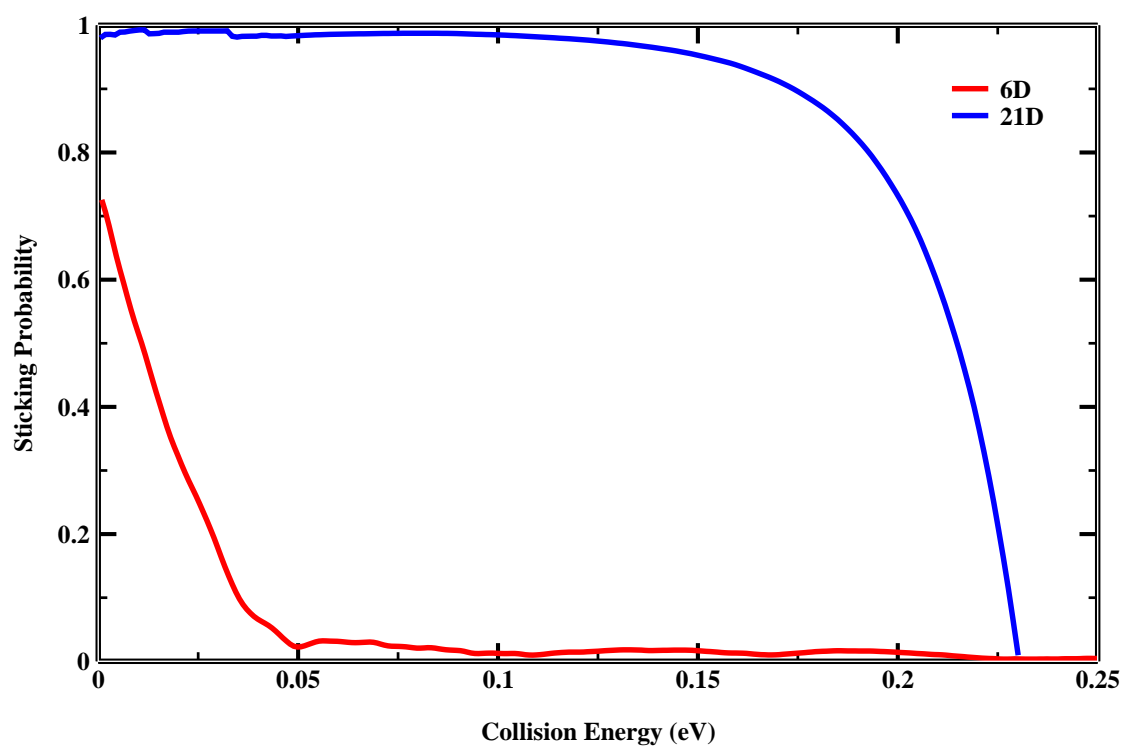


FIG. 8: CO/Cu, 21D MCCPD